Mechanics of Materials 83 (2015) 110–121

Contents lists available at ScienceDirect

Mechanics of Materials

journal homepage: www.elsevier.com/locate/mechmat

Determination of effective elastic properties of ferritic ductile cast iron by computational homogenization, micrographs and microindentation tests

Diego O. Fernandino *, Adrián P. Cisilino, Roberto E. Boeri

INTEMA – Faculty of Engineering, National University of Mar del Plata – CONICET, Av. Juan B. Justo 4302, Mar del Plata B7608FDQ, Argentina

ARTICLE INFO

Article history:
Received 18 August 2014
Received in revised form 18 December 2014
Available online 12 January 2015

Keywords:
Ferritic ductile iron
Computational homogenization
Microindentation
Elastic properties

ABSTRACT

A comprehensive procedure for the prediction of the elastic behavior of ferritic ductile iron by means of multiscale analysis is introduced in this work. The procedure combines computational procedures for the homogenization analysis, micrographic analysis to retrieve the geometries for the finite element analysis, and microindentation tests to assess the elastic behaviors of the different phases of the microstructure. The size of the representative volume element (RVE) is assessed in terms of geometrical descriptors of the microstructure (graphite fraction and nodule count and size) and the invariance and isotropy of the homogenized elastic responses. The RVE is sized to contain at least 50 nodules, and it results from 100× micrographs. The results for the homogenized values for the Young's modulus and the Poisson's ratio are found in excellent agreement to the data retrieved from tensile tests, values reported in the bibliography and analytical formulas available in the literature. The proposed procedure can be easily extended to the characterization of cast irons with more complex microstructures.

1. Introduction

Cast irons are materials consisting in a continuous metal matrix with disperse graphite and/or carbide inclusions. Their properties are determined by their microstructures, which are the result of the solidification process and the subsequent heat treatments. Graphite is the stable form of pure carbon in cast iron. The shape, size and spatial arrangement of graphite in the microstructure, which can range from flakes (gray irons) to spheroids (ductile iron), dramatically affects the mechanical properties of cast irons. The graphite flakes provide excellent damping characteristics to gray irons, but they also act as stress raisers, which cause localized plastic flow at low stresses that conducts to fragile failure. In turn, the graphite nodules, which act as crack arresters, are responsible for the excellent mechanical performance of ductile cast irons (Warda, 1990).

Ductile irons (DI) allow for a wide range of mechanical properties via microstructure control. Because of their good mechanical performance and relatively low cost when compared to steels, ductile cast irons are increasingly applied in the construction of high stressed parts for machines and vehicles. DIs are labeled based on the nature of their matrices: ferritic, pearlitic, martensitic, austempered and austenitic among others. Ferritic DI (FDI) is usually used to replace low-carbon steel when ductility and good impact properties are required in marine applications, valves, fittings, truck and agricultural implements and automotive steering knuckles. FDI is typically obtained by an annealing heat treatment consisting of an austenitizing stage followed by a slow cooling down (Warda, 1990; Labrecque and Cagne, 1998).

* Corresponding author. Tel.: +54 (0223) 4816600; fax: +54 (223) 481 0046.
E-mail address: dfernandino@fi.mdp.edu.ar (D.O. Fernandino).

http://dx.doi.org/10.1016/j.mechmat.2015.01.002
0167-6636/

During the solidification process of DI, graphite and austenite nucleate independently into the liquid, with the austenite growing dendritically. As the solidification process advances, the austenite dendrites trap the surrounding nodules. Further growth of the graphite nodules takes place by carbon diffusion from the liquid to the nodules through the austenite envelope. Consequently, one dendrite contains several nodules. The resulting solidification structure is formed by multinodular solidification units commonly called eutectic cells, which are separated by regions called cell boundaries. The first to freeze zones, coincident with the axes and arms of the austenite dendrites, are usually named FTF. As the solid phases grow and collide with neighboring growing units, the last portions of remaining melt locate between them, and are referred to as the Last to Freeze zones (LTF) (Rivera et al., 2002, 1995). The solidification structure can be revealed from the microsegregation patterns of the alloy elements. In particular, elements dissolved substitutionally in austenite and ferrite, such as Si and Mn, have low diffusivity in the solid phase, so their segregation patterns originated during the solidification will change very little during cooling to room temperature and with subsequent heat treatments. In this context, the microsegregations can be measured qualitatively by using a number of techniques, such as microanalysis (Boeri and Weinberg, 1993; Rivera et al., 1988; Kostyleva et al., 1992) or metallographic techniques (Motz, 1988; Zhou et al., 1993). The effectiveness of several metallographic techniques were evaluated by Rivera et al. (1995), who applied a color reagent sensitive to microsegregation that provides the best results to reveal the solidification structure of FDI. Fig. 1 depicts an FDI micrograph after color etching where the graphite nodules, FTF and LTFs are marked. Given the fact that LTF zones solidify at the end of the process, certain alloy elements and impurities may diffuse and concentrate or be depleted in these zones. In addition, the natural volume change associated to solidification can induce the formation of small shrinkage cavities at the LTF (Rivera et al., 1995, 1999).

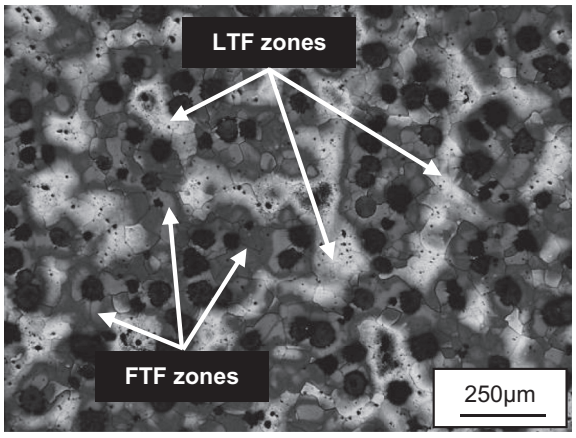

Fig. 1. FDI micrograph after color etching: spheroidal graphite nodules (black), FTF zones (dark zones) and LTF zones (bright zones).

The characterization of the FDI microstructure needs of geometrical and material-behavior constitutive data. The geometrical description is typically given in terms of graphite volume fraction, nodularity (a measure of the nodule sphericity) and nodular count (the number of nodules per unit area). In general, higher nodular counts and nodularities promote better mechanical properties (Burditt, 1992; http://www.ductile.org, 0000). In what respects to the material-behavior constitutive data, the usual assumption is to assimilate the matrix as homogeneous (Bonora and Ruggiero, 2005; Ghosh and Moorthy, 1995; Carazo et al., 2014; Hollister and Kikuchi, 1994; Hashin, 1983; Ortiz et al., 2001a; Basso et al., 2009; Kosteski et al., 2011; Ortiz et al., 2001b). However, the experimental evidence shows that the matrix presents a high degree of heterogeneity (see Fig. 1). The assessment of the associated heterogeneity in the mechanical properties needs experimental analysis at the microstructural level.

Computational micromechanics provides valuable tools to help to the better understanding of DI mechanical behavior. Finite, boundary and discrete element methods have been used to study the DI effective elastic response (Bonora and Ruggiero, 2005; Carazo et al., 2014) fatigue crack propagation (Ortiz et al., 2001a) and fracture (Bonora and Ruggiero, 2005; Basso et al., 2009; Kosteski et al., 2011). The hypotheses used in the geometrical description of the microstructure play a key role point when dealing with computational models. There are three approaches to account for the size and spatial distribution of the nodules: they are assumed to be of one size and periodically located (Bonora and Ruggiero, 2005), they are artificially generated by means of computer algorithms (Ortiz et al., 2001a; Basso et al., 2009; Kosteski et al., 2011; Ortiz et al., 2001b) or they are directly extracted from actual micrographs (Carazo et al., 2014). Analysis based on periodic microstructures are suitable to elaborate qualitative descriptions of the material behavior, but as it has been shown by Kosteski et al. (2011), they may conduct to erroneous results, especially when non-linear phenomena are involved. The simulations of non-periodic microstructures are based on homogenization analyses of Representative Volume Elements (RVE) (Hollister and Kikuchi, 1994; Zohdi and Wriggers, 2000). Among the various definitions available in the literature (Hashin, 1983; Willis, 2002; Kanit et al., 2003), the RVE is assimilated in this work to the minimum volume of material whose behavior is equivalent to that of a volume of a homogeneous fictitious material.

The present work is focused in developing a comprehensive procedure for the prediction of the elastic behavior of FDI. The procedure is based on the computational asymptotic homogenization of RVEs. The geometry of the RVEs is taken from actual micrographs, as this procedure offers a better chance to simulate more complex matrix microstructures and graphite morphologies and distributions, and, very importantly, to contemplate future simulations of nonlinear phenomena that demand detailed information about the microstructure. The non-homogeneity in the mechanical properties of the different microstructural phases is experimentally assessed by means of

microindentation tests. The size of the RVE is assessed in terms of geometrical descriptors of the microstructure (graphite fraction and nodule count and size) and the invariance and isotropy of the homogenized elastic responses. The homogenized elastic properties are validated by comparison to the Young's modulus data retrieved from tensile tests

2. Materials and methods

2.1. Materials

MEGAFUND S.A provided FDI samples. Their chemical composition, listed in Table 1, was determined by means of a Baird DV6 spectrometer. The samples were one-inch 'Y' blocks cast in sand molds (ASTM A897M). All blocks were ferritized by an annealing heat treatment, consisting of an austenitizing stage at 920 °C for 4 h, followed by a slow cooling down to room temperature inside the furnace. Metallographic samples were prepared using standard polishing methods. Etching was carried out using nital (2%). The microconstituents, the nodule count, nodularity and nodule size were quantified using an OLYMPUS PMG3 optical microscope and the Image Pro Plus software (Image Pro-Plus Software, 2012).

The results for the microstructural characterization (ASTM A 247) and the Brinell hardness tests (ASTM E10-01) in the as-cast condition are listed in Tables 2 and 3, respectively. The reported values are, in every case, the average of at least three measurements. Fig. 2 shows micrographs of the material microstructures in the as-cast condition and after the annealing heat treatment. Note the transformation of the fully pearlitic matrix in the as-cast condition (Fig. 2a) to fully ferritic with a small amount of globular pearlite after the annealing heat treatment (Fig. 2b).

2.2. Methods

2.2.1. Microindentation tests

Three zones were distinguished in the FDI microstructure: ferrite, LTF and graphite nodules. The three zones were considered to behave as isotropic linear-elastic solids. A set of metallographies of the FDI microstructure were color etched using a reagent sensitive to the segregation of Si (Rivera et al., 1995) (10 g NaOH, 40 g KOH, 10 g picric acid and 50 ml distilled water) to distinguish the three zones, see Fig. 3a. The etchant was applied when boiling at 120 °C and the etching time was about 90 s. The metallographies were inspected to select three zones that were representative of the microstructure topology.

The Young moduli of the three zones were measured by means of microindentation tests using the Oliver and Pharr method (Oliver and Pharr, 1992). The tests were performed using a Tl900 SERIES Hysitron equipped with the MRNP Multirange nanoprobe®, and a Vikers indenter. The indentations were done in rectangular patterns as it is depicted in Fig. 3b. All tests were performed in displacement-control mode with the loading curve in Fig. 4. The maximum displacement of 1 μm was selected in order to obtain an imprint size that allowed practicing 25 indentations over the analysis zone.

Table 1
Chemical composition of DI (wt%).

C	Si	Mn	S	P	Mg	Cu	Ni	Cr
3.32	2.36	0.31	0.012	0.016	0.033	0.62	0.025	0.058

Table 2
Metallographic characterization of as-cast samples (ASTM A 247).

Nodule count [nodules/mm^2]	Nodularity	Nodule size
100	>95%	6

Table 3
Hardness value of as-cast and ferritized samples.

Matrix	Label	Brinell hardness
Ferritic	C1F	149
As-cast (pearlitic)	AC	272

2.2.2. Micrographic analysis

The micrographic analysis was used to characterize the nodule shapes and spatial distributions. Metallographic samples were obtained from the *Y*-block as it is illustrated in Fig. 5 and mounted in bakelite for observation. An example of a typical micrograph is illustrated in Fig. 6a. The micrographs were binarized using Image Pro-Plus (2012) to distinguish the matrix and the graphite nodules, see Fig. 6b. The resulting images were used to perform the nodule count and to measure the nodule area, diameter, perimeter and roundness as is shown in Fig. 6c. The data was analyzed in terms of the nodule size class (SC) according to ASTM A247. The above data was used to size the RVE. With this purpose, a set of analyses with 50×, 100×, 200× and 500× magnifications were analyzed (see Fig. 7). The associated observation areas ranged from 8820 μm^2 (500×) to 854,539 μm^2 (50×). Twenty different observation fields at random positions were considered for each magnification.

2.2.3. Tensile tests

Tensile tests were performed on sub-size test samples (ASTM A897M-03), which were machined from the same zone of the *Y*-blocks where the metallographic samples were extracted. Tensile tests were conducted according to the specifications of ASTM E8M-04 using 30-ton Morh & Federhaff test machine and a MTS (632.11F-20) extensometer.

2.2.4. Computational homogenization

2.2.4.1. Formulation. The computational homogenization analysis uses the asymptotic method as it is introduced in Hollister and Kikuchi (1992). The method considers two scales: the macro-scale for the continuum of which the homogenized elastic properties are computed, and the micro-scale for the material microstructure, see Fig. 8. The method assumes that the separation between

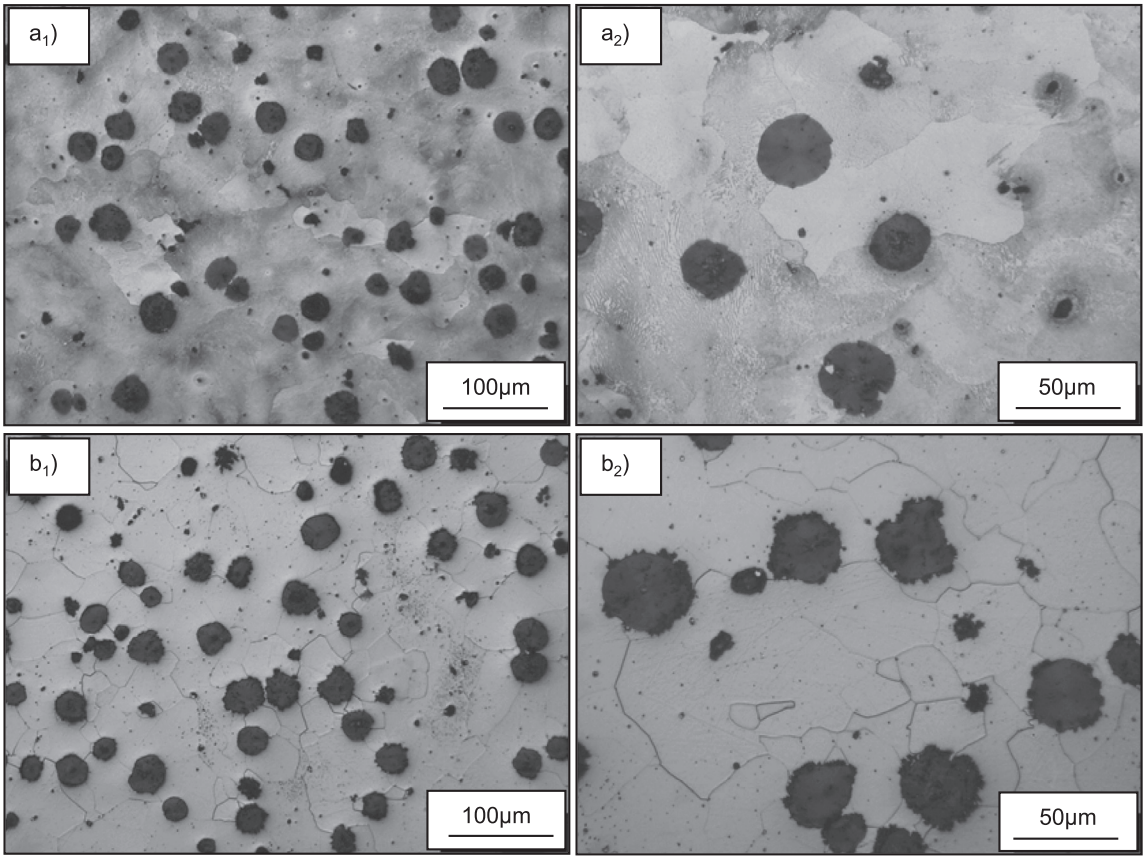

Fig. 2. Optical micrographs for the material in the (a) as cast condition and (b) after the annealing heat treatment.

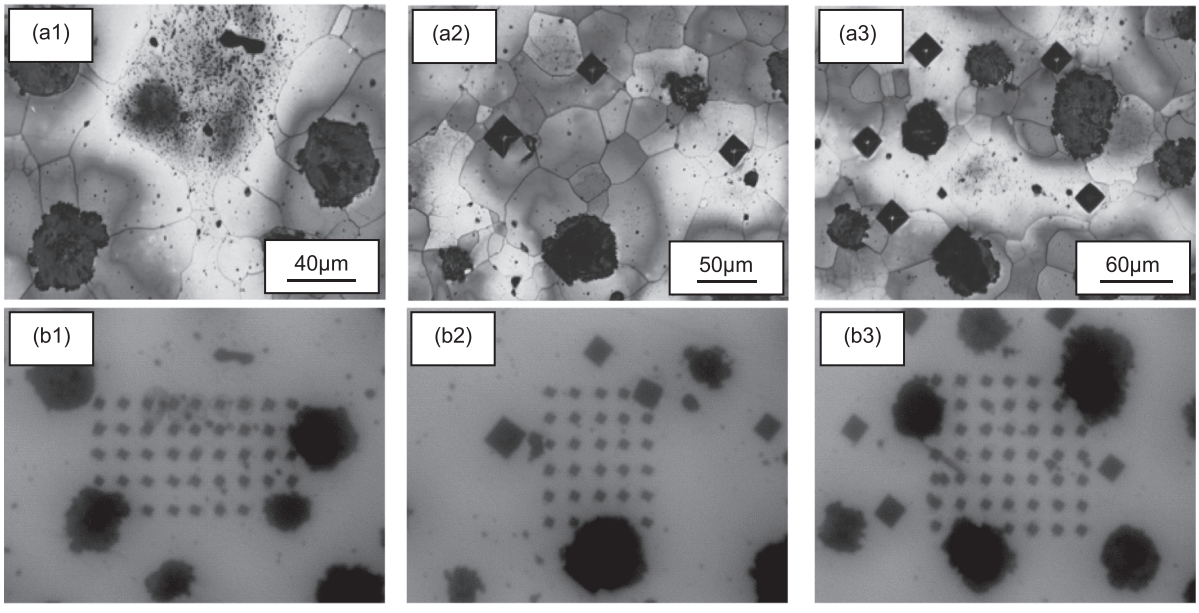

Fig. 3. Microindentation tests: (a) material microstructure revealed after color etching (LTF zones are revealed bright) and (b) microindentation patterns.

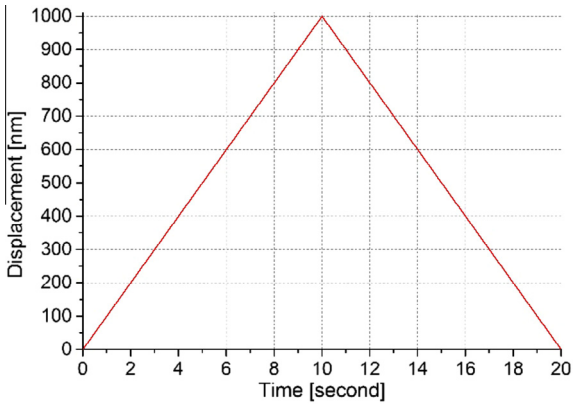

Fig. 4. Loading curve for the microindentations tests.

the scales, this is, the characteristic length of the micro-scale l, say the nodule size, is much smaller than the characteristic length of the macro-scale L.

It is also assumed that the material has linear-elastic responses in both, the macro and the micro scales. The relationship between the stress and strains in the macro-scale is given in terms of the homogenized stiffness tensor $\mathbb{C}$ such that

$$\sigma = \mathbb{C}\varepsilon, \tag{1}$$

where the macroscopic fields can be computed as the volume average of their microscopic counterparts over the domain of the RVE, this is:

$$\sigma = \frac{1}{V_{\mathrm{RVE}}}\int_{V_{\mathrm{RVE}}} \sigma_\mu dV \quad \text{and} \tag{2}$$

$$\varepsilon = \frac{1}{V_{\mathrm{RVE}}}\int_{V_{\mathrm{RVE}}} \varepsilon_\mu dV. \tag{3}$$

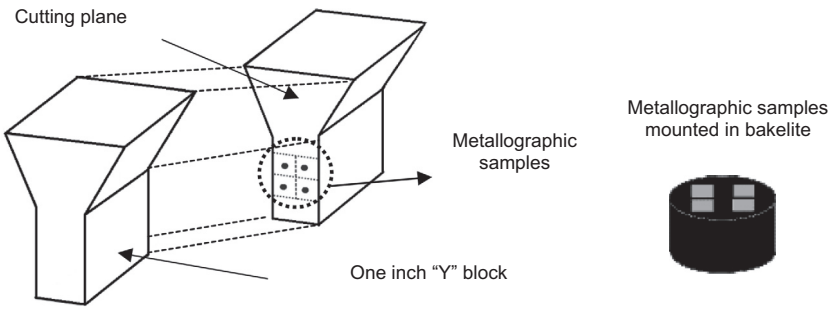

Fig. 5. Methodology to obtain the metallographic samples for the analysis.

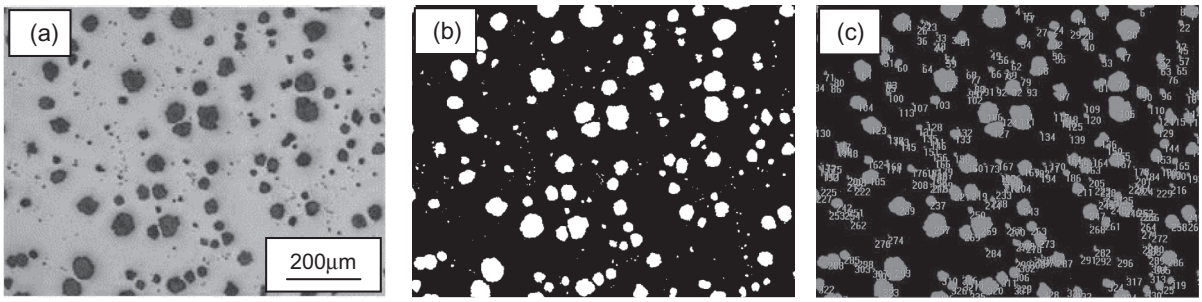

Fig. 6. Optic metallography of FDI (50×): (a) original image, (b) processed image, and (c) results of the analysis of the nodules.

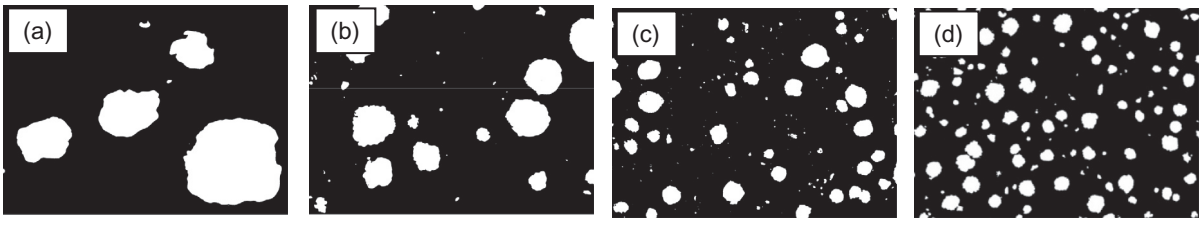

Fig. 7. Examples of the analysis areas for the different magnifications: (a) 500×; (b) 200×; (c) 100×; (d) 50×.

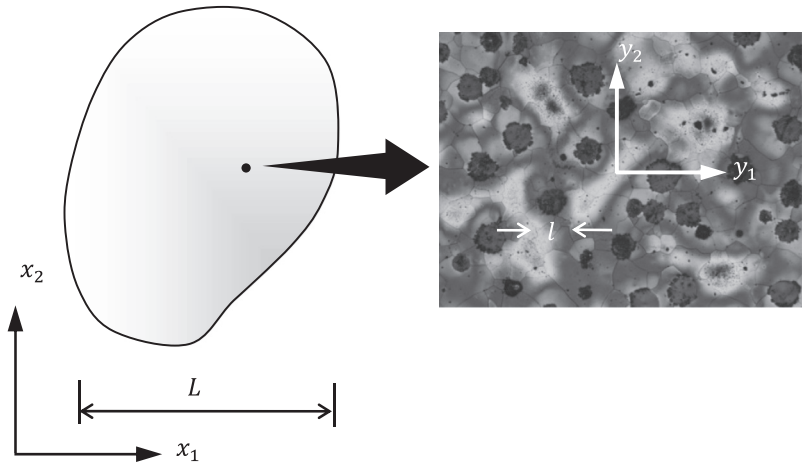

Fig. 8. Macro continuum with a local RVE.

Microscopic stress and strains in the RVE are related such that

$$\sigma_\mu = \mathbb{C}_\mu \varepsilon_\mu. \tag{4}$$

Without loss of generality, the displacement field in the microscale, u_μ, is assumed to be decomposed as:

$$u_\mu(y) = u + \bar{u}(y) + \tilde{u}_\mu(y), \tag{5}$$

where u is the displacement in the macro-scale,

$$\bar{u}(y) = \varepsilon \cdot y, \tag{6}$$

is linear in the RVE coordinate y, and $\bar{u}_\mu$ is a fluctuation of the displacement. The microscopic strain field associated to the displacement field in Eq. (4) is

$$\varepsilon_\mu = \varepsilon + \tilde{\varepsilon}_\mu \tag{7}$$

Although the asymptotic homogenization method is rigorously valid for periodic microstructures, i.e. those composed by repeated unit cells in the domain, Terada et al. (2000) showed that periodic boundary conditions could be applied to non-periodic heterogeneous media to get estimates of the mechanical properties. In fact, they showed that results obtained by means of other boundary conditions converge to the results obtained using periodic boundary conditions when the size of the sample is big enough. Similar conclusions have been reported by Carazo et al. (2014), who investigated the effects of the RVE shape and boundary conditions on the elastic homogenization of cast iron.

In general, the strain field in the macro-scale is not known a priori. However, since the problem is linear, any arbitrary ε may be written as a linear combination of unit strains, which are defined as

$$\varepsilon^{11}_{pm} = \begin{bmatrix} 1 & 0 \\ 0 & 0 \end{bmatrix}, \quad \varepsilon^{22}_{pm} = \begin{bmatrix} 0 & 0 \\ 0 & 1 \end{bmatrix} \quad \text{and} \quad \varepsilon^{12}_{pm} = \begin{bmatrix} 0 & 1 \\ 1 & 0 \end{bmatrix} \tag{8}$$

Once the three microscopic strain states are known, the local structure tensor $\mathbb{M}_{ijpm}$, which relates the macroscopic strain ε^{kl}_{pm} and the microstructural total strain $\varepsilon^{kl}_{\mu_{ij}}$, is calculated using

$$\varepsilon^{kl}_{\mu_{ij}} = \mathbb{M}_{ijpm} \varepsilon^{kl}_{pm}. \tag{9}$$

Once $\mathbb{M}$ is known, the local strain at any point within the RVE may be calculated from an arbitrary homogeneous macroscopic strain as

$$\varepsilon_\mu = \mathbb{M}\varepsilon. \tag{10}$$

The homogenized elasticity tensor $\mathbb{C}$ may also be calculated from $\mathbb{M}$. Starting from Hooke's law at the microscopic level (4), both sides are integrated over the RVE and divided by the total RVE volume to give

$$\frac{1}{V_{\text{RVE}}} \int_{V_{\text{RVE}}} \sigma_\mu dV = \frac{1}{V_{\text{RVE}}} \int_{V_{\text{RVE}}} \mathbb{C}_\mu \varepsilon_\mu dV. \tag{11}$$

Substituting for ε_μ from (10) and recalling (2) and (3) gives

$$\sigma = \left(\frac{1}{V_{\text{RVE}}} \int_{V_{\text{RVE}}} \mathbb{C}_\mu \mathbb{M} dV \right) \varepsilon, \tag{12}$$

where the homogenized stiffness tensor is

$$\mathbb{C} = \frac{1}{V_{\text{RVE}}} \int_{V_{\text{RVE}}} \mathbb{C}_\mu \mathbb{M} dV. \tag{13}$$

The homogenized stiffness tensor $\mathbb{C}$ is, in general, anisotropic. On the other hand, experimental evidence shows that FDI presents an isotropic response in the macroscale. Thus, it is proposed to recover the Young's modulus of and the Poissońs ratio of the FDI from the isotropic part of $\mathbb{C}$, and to use the anisotropy of $\mathbb{C}$ as an indicator of the representativeness of the result.

Among other choices (Browaeys and Chevrot, 2004; Dinçkal and Akgöz, 2010; Ta et al., 2010), the tensor $\mathbb{C}^{iso}$ of an isotropic material for the two-dimensional plane-strain condition can be written using the bulk modulus κ and shear modulus μ:

$$\mathbb{C}^{iso} = 2\kappa\mathbb{S} + \sqrt{5}\mu\mathbb{D} \tag{14}$$

where $\mathbb{S}$ and $\mathbb{D}$ are respectively the so-called normalized spherical tensor and deviatoric tensor, defined for the two-dimensional plane-strain condition as

$$\mathbb{S} = \frac{1}{2}\begin{bmatrix} 1 & 1 & 0 \\ 1 & 1 & 0 \\ 0 & 0 & 0 \end{bmatrix} \tag{15}$$

and

$$\mathbb{D} = \frac{1}{\sqrt{5}}\begin{bmatrix} 1 & -1 & 0 \\ -1 & 1 & 0 \\ 0 & 0 & 1 \end{bmatrix}. \tag{16}$$

Tensors $\mathbb{S}$ and $\mathbb{D}$ are an orthogonal pair for the scalar product associated to the Frobenius norm. Then, the closest equivalent isotropic stiffness tensor to $\mathbb{C}$, which is denoted as $\mathbb{C}_{eq}^{iso}$, can be computed by projection as follows

$$2\kappa_{eq}^{iso} = \langle \mathbb{C}, \mathbb{S} \rangle, \tag{17}$$

$$\sqrt{5}\mu_{eq}^{iso} = \langle \mathbb{C}, \mathbb{D} \rangle \tag{18}$$

and

$$\mathbb{C}_{eq}^{iso} = 2\kappa_{eq}^{iso}\mathbb{S} + \sqrt{5}\mu_{eq}^{iso}\mathbb{D}. \tag{19}$$

The symbols κ_{eq}^{iso} and μ_{eq}^{iso} in the above equations are the bulk and shear moduli of the equivalent isotropic tensor. Under a plane strain conditions, the equivalent bulk and shear moduli are related to the Young's modulus and the Poisson's coefficient via

$$\kappa_{eq}^{iso} = \frac{E}{2(1-2\nu)(1+\nu)} \tag{20}$$

and

$$\mu_{eq}^{iso} = \frac{E}{2(1+\nu)}. \tag{21}$$

Finally, the index proposed by Ta et al. (2010), belonging to $[0, 1]$, is used to asses the anisotropy of the homogenized elastic tensor,

$$I_a = \sqrt{\frac{\left\| \mathbb{C} - \mathbb{C}_{eq}^{iso} \right\|_F^2}{\|\mathbb{C}\|_F^2}}, \tag{22}$$

where $||\cdot||_F^2$ denotes the Frobenius norm.

2.2.4.2. Implementation. The above procedure was implemented in the context of FEA and coded using Matlab. The microscopic strain fields for the three unit strains in Eq. (8) were computed by means of finite element models of rectangular-shaped RVEs. The model geometries were produced automatically from the micrographs in Section 2.2.2. The models were discretized using regular quadrilateral linear elements, see Fig. 9. The elastic behavior in the microstructure was assumed isotropic for all the phases. The value of $\mathbb{C}_\mu$ for each element was set depending if it lies at the loci of the matrix or of a graphite nodule according to the results of the micro indentation tests (see Section 3.1 below). All the models used in this work were discretized using an element $\varepsilon_{\mu_{ij}}^{kl}$ size equal to 1 μm. This element size ensures the discretization of the smallest nodules (class 8) with 13 elements along the diameter. The mesh-independence of the results was confirmed by means of convergence analysis.

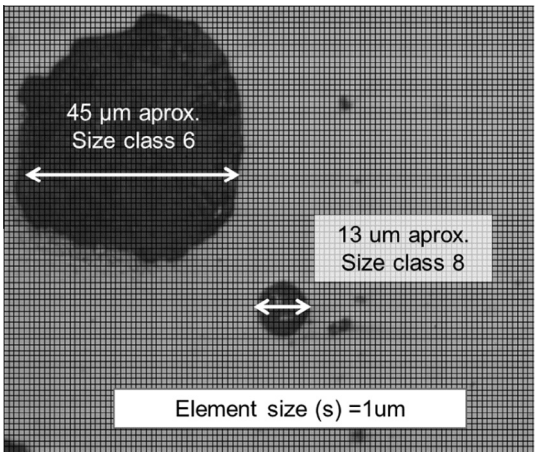

Fig. 9. Detail of an RVE discretized with an element size of $s = 1$ μm.

Displacement boundary conditions for load cases in Eq. (8) were specified as in Eq. (6). The periodicity of the displacement fields was enforced using the approach due to Barbero (2008).

The structure tensor $\mathbb{M}$ was computed at the element centroids using Eq. (9). To this end, a system of equation was set for each of the load cases using the macroscopic strains ε_{pm}^{kl} and their corresponding in the microscale:

$$\begin{Bmatrix} \varepsilon_{ij}^{11} \\ \varepsilon_{ij}^{22} \\ \varepsilon_{ij}^{12} \end{Bmatrix} = \begin{bmatrix} \varepsilon_{\mu 11}^{11} & \varepsilon_{\mu 22}^{11} & 2\varepsilon_{\mu 12}^{11} \\ \varepsilon_{\mu 11}^{22} & \varepsilon_{\mu 22}^{22} & \varepsilon_{\mu 12}^{22} \\ \varepsilon_{\mu 11}^{12} & \varepsilon_{\mu 22}^{12} & \varepsilon_{\mu 12}^{12} \end{bmatrix} \begin{Bmatrix} \mathbb{M}_{ij11} \\ \mathbb{M}_{ij22} \\ \mathbb{M}_{ij12} \end{Bmatrix}. \tag{23}$$

Once $\mathbb{M}$ was known, the homogenized stiffness tensor was calculated using the discrete version of Eq. (13):

$$\mathbb{C} = \frac{1}{\sum_{p=1}^{N} V_i} \sum_{p=1}^{N} \mathbb{C}_\mu^p \mathbb{M}^p V_i, \tag{24}$$

where is N is the number of elements of finite element model and V_i are their volumes.

The equivalent isotropic stiffness tensor, $\mathbb{C}_{eq}^{iso}$, was computed using Eqs. (15)–(19). This result was then used to recover the homogenized values for the Young's modulus and the Poisson's coefficient, E and ν, from Eqs. (20) and (21), respectively. Finally, the anisotropy index of the homogenized elastic tensor was computed using expression (22).

3. Results and discussion

3.1. Micrographic analysis

The results of the micrographic analysis are given in Table 4. The nodular count and the graphite area fraction as a function of the size of the sample area are plotted in Fig. 10. The nodule diameter associated to the SC 8, 7 and 6 are 15 μm, 30 μm and 50 μm, respectively. It can be observed that the graphite area fraction and the nodular count increase with reduction the sample area.

Table 4
Results of the micrographic analysis.

	Sample area [μm²]	Nodules quantified	Aspect ratio (a_r)	Graphite area fraction (c_i) [%]	Nodular count [nod/mm²]	SC8 [%]	SC7 [%]	SC6 [%]
50×	854,539	114 ± 10%	1.28 ± 0.26	9,5 ± 1.4	145 ± 12	28 ± 3	52 ± 5	20 ± 2
100×	213,634	56 ± 15%	1.24 ± 0.24	10 ± 1.5	178 ± 13	29 ± 9	56 ± 10	15 ± 7
200×	53408	15 ± 19%	1.24 ± 0.26	12 ± 2.2	206 ± 18	29 ± 14	59 ± 20	12 ± 8
500×	8545	4 ± 41%	1.25 ± 0.27	15 ± 4.6	295 ± 33	30 ± 23	62 ± 33	8 ± 16

Consequently, the number of quantified nodules decreases. In every case, dispersions diminish with the increment of the observation area. Both, the nodular count and the graphite area fraction tends to stabilize at a sample area of approximately 213,600 μm², but this stabilization is more evident in the graphite area fraction. In this sense, assuming that all the carbon content in the material is concentrated in the nodules, the graphite area fraction might be used as an indicator for the RVE size.

3.2. Micro-indentation tests

Fig. 11 depicts some of the load vs displacement curves for the micro-indentations practiced in FTF, LTF and graphite nodules. The associated results for the Young's moduli are reported in the histograms in Fig. 12(a) and (b). The mean values and standard deviations of the Young's moduli are

$$E_{\text{nodule}} = 15 \pm 0.15 \text{ GPa}, \tag{25}$$

$$E_{\text{FTF}} = 230 \pm 8.22 \text{ GPa} \tag{26}$$

and

$$E_{\text{LTF}} = 255 \pm 7.77 \text{ GPa}. \tag{27}$$

It can be observed that while there is a great contrast between the behaviors of the graphite nodules and the two zones in the matrix, FTF and the LTF behave very similarly. Based on the above results, the FTF and the LTF phases were assimilated to a single material, say the metallic matrix, with its Young's modulus computed as

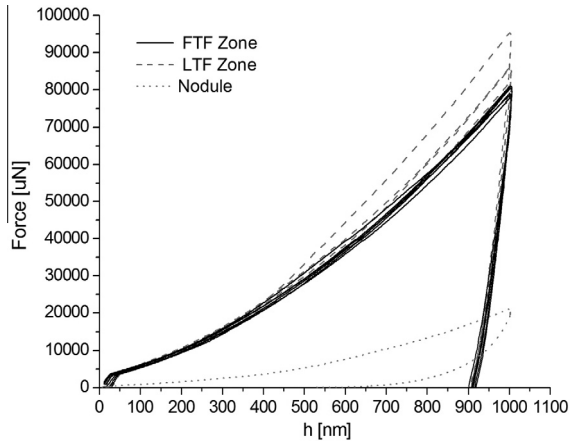

Fig. 11. Some of the load vs displacement curves from the micro indentations practiced in ferrite, LTF and graphite nodules.

the area-weighted average of the FTF and LTF data. The area fraction values for the FTF and the LTF were measured by digital image processing of the etched RVE images. The results were 78% of FTF and 22% of LTF, with a dispersion less than 2%, see Fig. 13. Thus Young's modulus for the metallic matrix resulted

$$E_{\text{matrix}} = 235 \pm 8 \text{ GPa}. \tag{28}$$

Note that the Young's modulus calculated in (28) is about 10% higher than conventional value used for a SAE1010 ferritic steel, this is 210 GPa. This discrepancy is

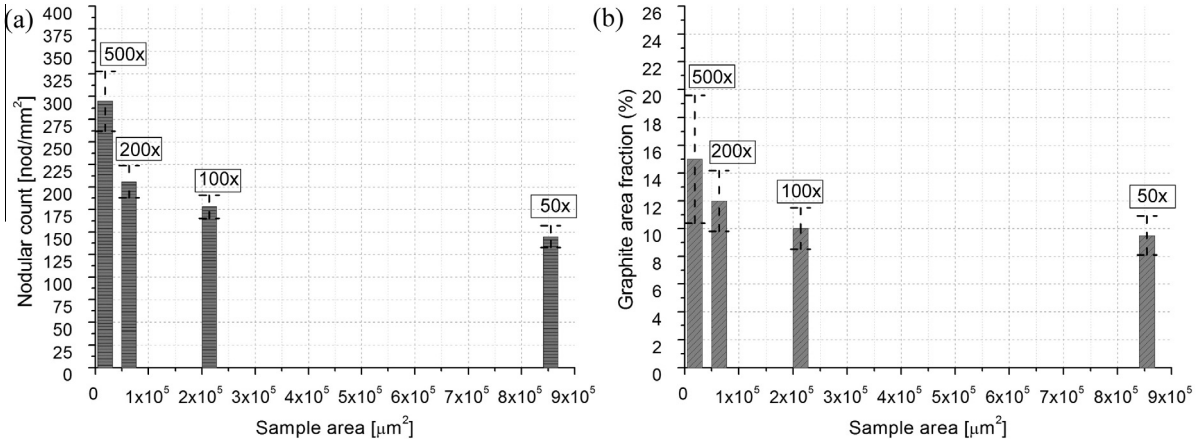

Fig. 10. Results for the (a) nodule count and (b) graphite area fraction. Error bars indicate dispersion of the results. The labels indicate the magnification associated to the analysis area.

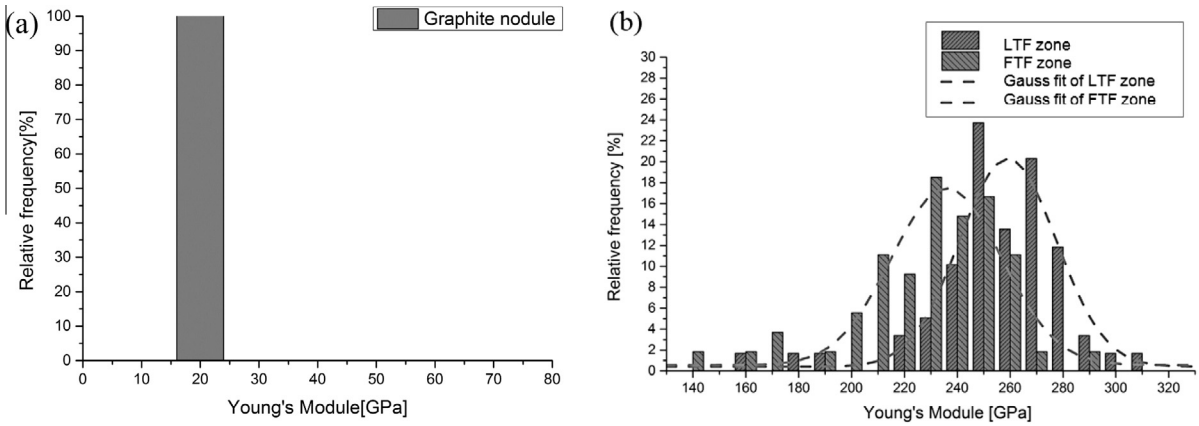

Fig. 12. Histograms with the results for the Young moduli: (a) nodules, (b) LTF and FTF.

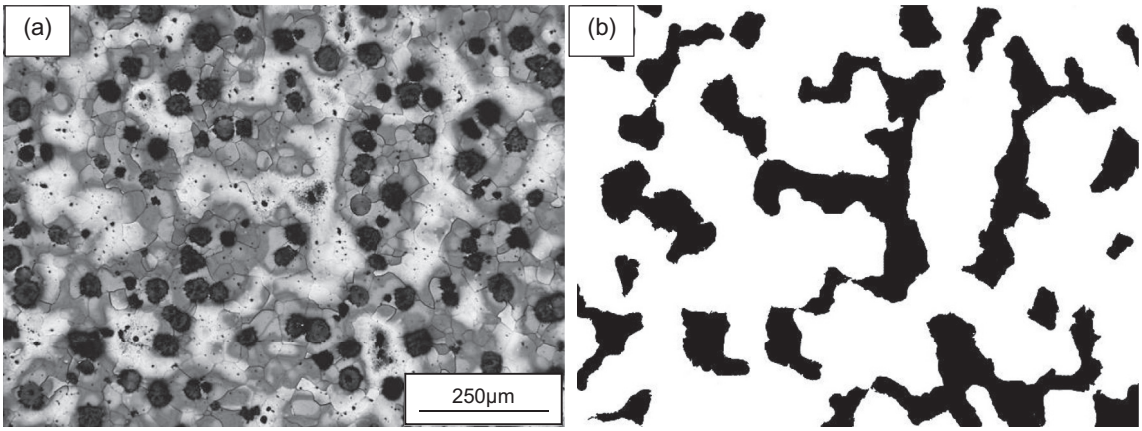

Fig. 13. Ferritic DI microstructure at 50× (a) revealed after color etching (b) binarized image of the metallic matrix, FTF (white) and LTF (black).

attributed to the presence of alloys in the composition of the FDI matrix, in contrast to the unalloyed steel. A constant value for the Poisson ratio $\nu = 0.28$ was used for both, the matrix and the nodules (Warda, 1990).

3.3. Tensile tests

Fig. 14 illustrates the stress vs. strain curve of one of the tensile tests. Experimental values for the Young's modulus, the yield stress and the ultimate tensile stress and strain are reported in Table 5. These values are the average of four tests. Data retrieved from the literature are also reported in Table 5 (Warda, 1990; Burditt, 1992). It can be observed that the results of the tests are in very good agreement to those of the references.

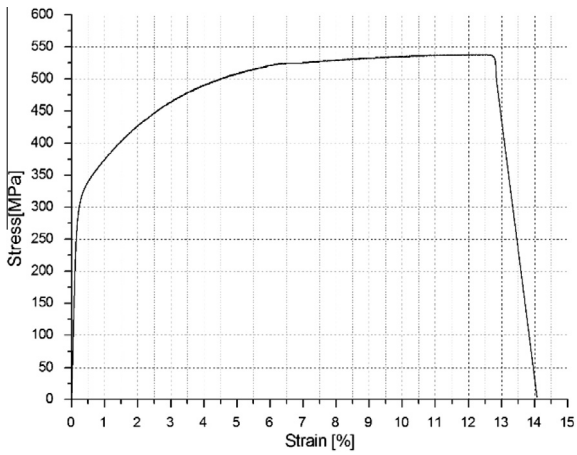

Fig. 14. Stress vs. strain response of a FDI tensile test.

3.4. Homogenization analysis

Fig. 15 depicts the results for the homogenized Young's modulus and Poisson's ratio in terms of the sample size. Each point in the plots is the average of six analyses; the error bars indicate the dispersion of the results. It can be observed that the values for both, *E* and *nu* converge towards constant values as the area of the samples increase. At the same time, the dispersion of the results monotonously diminishes with the increment of the area of the sample.

Table 5
Experimental results from tensile test.

	Yield stress $\sigma_{0.2}$ [MPa]	Ultimate tensile stress σ_{UTS} [MPa]	Ultimate tensile strain ε_{UTS} [%]	Young's module E [GPa]	Poisson's ratio ν
Experimental results	329	536	12,5	172 ± 6	–
Bibliographic sources (Warda, 1990; Burditt, 1992)	310	562	12–17	169	0.28

The dependence of the results with the sample size is also addressed in terms of anisotropy. The results for the anisotropy index, I_a, are given in Fig. 16. It can be observed that, like for E and ν above, the index converges and its dispersion diminishes with increment of the sample size.

The above results allow observing that samples larger than 0.213 mm^2 (this is, those corresponding to 100× magnification) result in the computation of size-independent isotropic elastic properties with tight levels of uncertainty. In other words, the RVE is asked to contain a minimum of 56 nodules (see Table 4).

The resultant homogenized stiffness tensor for the RVE is $I_a = 0.311$

$$\mathbb{C} = \begin{bmatrix} 210.7741 & 84.2964 & 0.4570 \\ 84.2936 & 215.2425 & -0.0080 \\ 0.1137 & 0.0001 & 63.8648 \end{bmatrix}. \quad (29)$$

The associated anisotropy index of which is $I_a = 0.00886 \pm 0.00226$. In order to quantitatively address this last result, consider for instance, that the value of the anisotropy index for an orthotropic elastic tensor with $E_1 = 2E_2$ is, for $E_1 = 1.2E_2$ is $I_a = 0.086$ and for $E_1 = 1.02E_2$ is $I_a = 0.009$.

The associated homogenized values for the Young's modulus and the Poisson's ratio of FDI are

$$E = 171 \pm 7 \text{ GPa} \quad (30)$$

and

$$\nu = 0.282 \pm 0.001 \quad (31)$$

respectively.

It results from the comparison of the results in (30) and (31) with the data in Table 5, that the mean value for the homogenized Young's modulus presents a discrepancy less than 2% with respect to the experimental value. Similarly, the discrepancy between the homogenized and reference values for the Poisson's ratio is less than 1%.

The result for the Young's modulus is also compared to that of the analytical estimation due to Boccaccini (1997), who used an analytical formulation developed by MAzilu and Ondracek (1990) to study the influence of the shape and volume fraction of graphite nodules on Young's modulus. The referred analytical solution is

$$E_{\text{Boccaccini}} = E_{\text{matrix}} \left\{ 1 - \frac{\pi}{9A} \left[9 - \frac{1}{1+1.99C} - \frac{3}{1+1.68C} - \frac{1/5}{1+1.04C} \right] \right\} \quad (32)$$

with

$$A = \frac{\left(\frac{4\pi}{C_i}\right)^{\frac{2}{3}} \left(\frac{z}{x}\right)^{-\frac{1}{3}}}{\sqrt{1 + \left(\left(\frac{z}{x}\right)^{-2} - 1\right) \cos^2 \alpha_i}}, \quad (33)$$

$$B = \left(\frac{4\pi}{c_i}\right)^{\frac{1}{3}} \left(\frac{z}{x}\right)^{\frac{1}{3}} \sqrt{1 + \left(\left(\frac{z}{x}\right)^{-2} - 1\right) \cos^2 \alpha_i} \quad (34)$$

and

$$C = \frac{1}{B} \left\{ \frac{E_{\text{matrix}}}{E_{\text{nodule}}} - 1 \right\}, \quad (35)$$

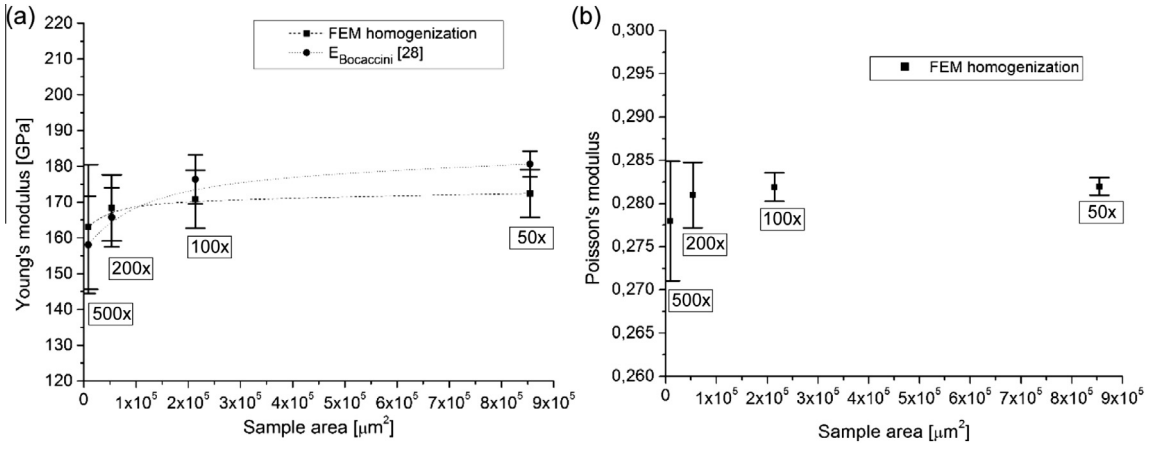

Fig. 15. Results for the (a) Young's modulus and (b) the Poisson's ratio as functions of the sample area. Error bars indicate the dispersion of the results. The labels indicate the magnification associated to the analysis area.

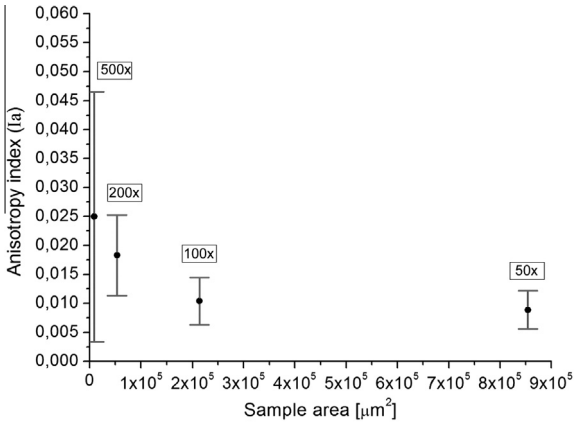

Fig. 16. Results for the anisotropy index as a function of the sample area. Error bars indicate the dispersion of the results. The labels indicate the magnification associated to the analysis area.

where $\cos^2\alpha_i$, which describes the orientation of the nodules, takes the value $\cos^2\alpha_i = 0.33$ in for the present case; c_i is fraction are of the graphite nodules; and z/x is the nodule aspect ratio. The expression (32) is evaluated in all analysis area (see Fig. 15a) using the experimental values for E_{matrix} and E_{nodule} in expressions (25) and (28), respectively; and the graphite volume fraction and the nodule aspect-ratio data from the micrographic analysis, see Table 4.

The resultant value corresponding to RVE size is

$$E_{\text{Boccaccini}} = 176 \pm 6\ \text{GPa}. \tag{36}$$

This value presents a deviation of 4% with respect to the results of the homogenization procedure.

4. Conclusions

This work introduces a comprehensive procedure for the prediction of the elastic behavior of ferritic ductile iron (FDI) by means of multiscale analysis. The procedure combines micrographic analysis to directly obtain the geometrical data for the micromechanical models, microindentation tests to measure the elastic properties in the microscale, and computational asymptotic homogenization analysis to compute the elastic response in the macroscale.

Microindentation analysis show that the two zones differentiated on the FDI matrix, fist-to-freeze zones and the last-to-freeze zones, have similar elastic behaviors, and so, they can be assimilated to a single matrix material. This result is in accordance to the usual hypothesis found in the literature.

The representative volume element (RVE) is sized in terms of the anisotropy of the homogenized macroscopic elastic tensor, and the invariance and dispersion of the homogenized values for the Young's modulus and the Poisson's ratio. In concordance with the results reported for the geometrical analysis of graphite nodule, where the graphite area fraction tends to stabilize at a sample area of 213,600 μm^2 approximately, it is concluded that a sample must contain, at least, a number of nodules of about 56 be assimilated to a RVE. Samples of this values result from 100× micrographs. RVEs of this size allow computing macroscopic elastic tensors with a degree of anisotropy less than 1%. The associated Young's modulus and the Poisson's ratio have dispersions of 4% and 1%, respectively.

In agreement to other works, see for instance Carazo et al. (2014), it was found that the influence of the RVE size is more noticeable in Young's modulus than in Poisson's ratio.

The homogenized values for the Young's modulus and the Poisson's ratio are in excellent agreement to experimental results used for validation. The deviations between the numerical predictions and the measurements are less than 2%. There is also a very good agreement, less that 5% difference, between the numerical predictions and the analytical estimations for the Young's modulus due to Boccaccini (1997).

The proposed procedure can be immediately applied to the elastic characterization of more complex microstructures, with more phases present in the microstructure; as they are the cases of pearlitic or ausferritic DI. It has also the potential to be extended to account for the non-linear responses at the microstructural scale.

Acknowledgements

This research has been supported by grants awarded by CONICET, ANPYCT and the National University of Mar del Plata. The authors wish to express their gratitude to MEGAFUND S.A for the provision of the material used in this study.

References

Barbero, E.J., 2008. Finite Element Analysis of Composite Materials. CRC Press, Boca Ratón, USA.

Basso, A., Martinez, R., Cisilino, A., Sikora, J., 2009. Experimental and numerical assessment of fracture toughness of dual-phase austempered ductile iron. Fatigue Fract. Eng. Mater. Struct. 33, 1–11. http://dx.doi.org/10.1111/j.1460-2695.2009.01408.x.

Boccaccini, A.R., 1997. Effect of graphite inclusions on the young's modulus of cast iron. Z. Metallkunde 88 (1), 23–26.

Boeri, R., Weinberg, F., 1993. Microsegregation of alloying elements in cast iron. Cast Met. 6, 153–158.

Bonora, N., Ruggiero, A., 2005. Micromechanical modeling of ductile cast iron incorporating damage. Part I: Ferritic ductile cast iron. Int. J. Solids Struct. 42, 1401–1424.

Browaeys, J.T., Chevrot, S., 2004. Decomposition of the elastic tensor and geophysical applications. Geophys. J. Int. 159 (2), 667–678. http://dx.doi.org/10.1111/j.1365-246X.2004.02415.

Burditt, F.M., 1992. Ductile Iron Handbook, American Foundrymen's Society Inc, Des Plaines, Illinois, USA, Section II, 31–34.

Carazo, F.D., Giusti, S.M., Boccardo, A.D., Godoy, L.A., 2014. Effective properties of nodular cast-iron: a multi-scale computational approach. Comput. Mater. Sci. 82, 378–390. http://dx.doi.org/10.1016/j.commatsci.2013.09.044.

Dinçkal, Ç., Akgöz, Y.C., 2010. Decomposıtıon of elastıc constant tensor ınto orthogonal parts. Int. J. Eng. Sci. Technol. 2 (6), 22–46.

Ghosh, S., Moorthy, S., 1995. Elastic–plastic analysis of arbitrary heterougeneous materials with the Voronoi cell finite element method. Comput. Methods Appl. Mech. Eng. 121 (1–4), 373–409.

Hashin, Z., 1983. Analysis of composite materials: a survey. J. Appl. Mech. 50 (3), 481–505.

Hollister, S.J., Kikuchi, N., 1992. A comparison of homogenization and standard mechanics analyses for periodic porous composites. Comput. Mech. 10, 73–95.

Hollister, S.J., Kikuchi, N., 1994. Homogenization theory and digital imaging: a bases for studying the mechanics and design principles of bone tissue. Biotechnol. Bioeng. 43 (7), 586–596.
<http://www.ductile.org/didata/Section3/3part1.htm>, # Effect of Graphite Shape.
Image Pro-Plus Software, 2012. Media Cybernetic. Retrieved from <http://www.mediacy.com>.
Kanit, T., Forest, S., Galliet, I., Mounoury, V., Jeulin, D., 2003. Determination of the size of the representative volume element for random composites: statistical and numerical approach. Int. J. Solids Struct. 40 (13/14), 3647–3679.
Kosteski, L., Iturrioz, I., Batista, R.G., Cisilino, A.P., 2011. The truss-like discrete element method in fracture and damage mechanics. Eng. Comput. 28 (6), 765–787. http://dx.doi.org/10.1108/02644401111154664.
Kostyleva, L.V., Ilyniski, V.A., Zhukov, A.A., 1992. Microsegregation of silicon in iron–carbon alloys. Cast Met. 5, 109–113.
Labrecque, C., Cagné, M., 1998. Review ductile iron: fifty years of continuous development. Can. Metall. Q. 37 (5), 343–378.
Mazilu, P., Ondracek, G., 1990. On the effective young's modulus of elasticity for porous materials. Part I: The general model equation. Thermal effects in fracture of multiphase materials. In: Proceedings of Euromechanic 255 Colloquium. Springer-Verlag, Paderborn, FRG, pp. 214–255.
Motz, J.M., 1988. Microsegregations-an easily unnoticed influencing variable in the structural description of cast materials. Prac. Met. 25, 285–293.
Oliver, W.C., Pharr, G.M., 1992. J. Mater. Res. 7 (6), 1564–1583.
Ortiz, J., Cisilino, A., Otegui, J., 2001a. Boundary element analysis of fatigue crack propagation micromechanisms in austempered ductile iron. Eng. Anal. Boundary Elem. 25 (6), 467–473, Retrieved from <http://www.sciencedirect.com/science/article/pii/S0955799701000340>.
Ortiz, J., Cisilino, A.P., Otegui, J.L., 2001b. Effect of microcracking on the micromechanics of fatigue crack growth in austempered ductile iron. Fatigue Fract. Eng. Mater. Struct. 4302, 591–605, Retrieved from <http://onlinelibrary.wiley.com/doi/10.1046/j.1460-2695.2001.00429.x/full>.
Rivera, G., Galarreta, I., Sikora, J., 1988. Proc. Int. Congr. ALAMET, 182–190.
Rivera, G., Boeri, R., Sikora, J., 1995. Revealing the solidification structure of nodular iron. Int. J. Cast Met. Res. 8 (1), 1–5.
Rivera, G., Boeri, R., Sikora, J., 1999. Int. J. Cast Met. Res. 11, 533–538.
Rivera, G., Boeri, R., Sikora, J., 2002. Revealing and characterizing solidification structure of ductile cast iron. Mater. Sci. Technol. 18, 691–698.
Ta, Q.-A., Clouteau, D., Cottereau, R., 2010. Modeling of random anisotropic elastic media and impact on wave propagation. Eur. J. Comput. Mech. 19 (1–2–3), 241–253.
Terada, K., Hori, M., Kyoya, T., Kikuchi, N., 2000. Simulation of the multi-scale con-vergence in computational homogenization approaches. Int. J. Solids Struct. 37 (16), 2285–2311.
Warda, R.D., 1990. Ductile Iron Data for Design Engineers. QIT-Fer et Titane Inc. Ductile Iron Group. Section II, 9–13.
Willis J.R., 2002. Mechanics of Composites. Lecture Notes: Ecolepolytechnique, fr., University of Cambridge.
Zhou, J., Zhong, F., Schmits, W., Engler, S., 1993. Application of a new color metallography technique to cast iron. Prakt. Metallogr. 30, 122–128.
Zohdi, T.I., Wriggers, P., 2000. On the sensitivity of homogenized material responses at infinitesimal and finite strains. Commun. Numer. Methods Eng. 16, 657–670.